ELSEVIER

Journal of Power Sources 84 (1999) 87–106

JOURNAL OF POWER SOURCES

www.elsevier.com/locate/jpowsour

A computational simulation of an alkaline fuel cell

Jang-Ho Jo, Sung-Chul Yi *

Department of Chemical Engineering, Hanyang University, Seoul 133-791, South Korea

Received 22 April 1999; received in revised form 25 May 1999; accepted 16 June 1999

Abstract

An advanced one-dimensional, isothermal mathematical model for a single cell of an alkaline fuel cell (AFC) is presented. Advances in an expression for the volume average velocity and in correlations and parameters are achieved. The parameters and operating conditions of the model are based on the Obiter Fuel Cell, which is employed as a power source for NASA space shuttles. A stimulated result is obtained that shows a close agreement with some of the experimental data. Profiles of variables, local overpotential and local current density are also obtained as a function of cell voltage. An investigation of the influence of initial electrolyte concentration shows that the performance of the AFC is maximized at a concentration of 3.5 M. Finally, it is found that increasing the operating pressure steadily enhances cell performance. © 1999 Elsevier Science S.A. All rights reserved.

Keywords: Alkaline fuel cells; Mathematical modeling; Single cell; Porous gas-diffusion electrode

1. Introduction

The alkaline fuel cell (AFC) has outstanding performance, efficiency and reliability among the various types of fuel-cell system and, thus, is still used by NASA to power spacecrafts. Moreover, Suljak [1] has recently reported a 12-fold enhancement in the performance of the AFC. It is expected that the most ideal type of fuel cell may be the anion (alkaline) exchange membrane fuel cell [2]. Hence, the future of the AFC still holds promise.

A mathematical model of a fuel cell provides a better understanding of the very complex phenomena that occur in such a system, as well as useful information. It also enables performance to be predicted as a function of design parameters and operating conditions. Nevertheless, the use of mathematical modelling of a gas-diffusion electrode is not pertinent to the detailed performance prediction of a single cell, since interactions between layers exist within the single cell. Hence, the need for mathematical modeling of the single cell is inevitable.

Mathematical models of an AFC single cell have been reported [3,4], but have some questionable aspects in the formulation of the equations, or are found to use invalid correlations and parameter values. Such deficiencies are corrected as much as possible in this study.

The single cell considered in this study consists of five layers and six boundaries. The model is composed of 11 variables, 25 governing equations and 38 boundary conditions to predict the following variables; partial pressure of hydrogen P_H, partial pressure of oxygen P_O, partial pressure of water vapour in the anode P_w^a, partial pressure of water vapour in the cathode P_w^c, concentration of dissolved hydrogen C_H, concentration of dissolved oxygen C_O, concentration of electrolyte C_e, solution phase potential Φ, volume average velocity $v^{\blacksquare}$, electrical potential of anode E_a, and electrical potential of cathode E_c. Additionally, the published specifications, such as catalyst loading, thickness of separator layer and operating conditions, of the Orbiter Fuel Cell (PC-17C) made by the International Fuel Cell (IFC) and which is employed as a power source for NASA space shuttles, are used as values of the base-case parameters for the prediction.

2. Description of system

The AFC single cell considered in this study consists of five layers, viz., are anode gas-diffusion layer, anode catalyst layer, separator layer, cathode catalyst layer, cathode gas-diffusion layer. A schematic diagram of the cell is

* Corresponding author. Tel.: +82-2-2290-0481; fax: +82-2-2298-1615; E-mail: scyi@email.hanyang.ac.kr

0378-7753/99/$ - see front matter
PII: S0378-7753(99)00309-2

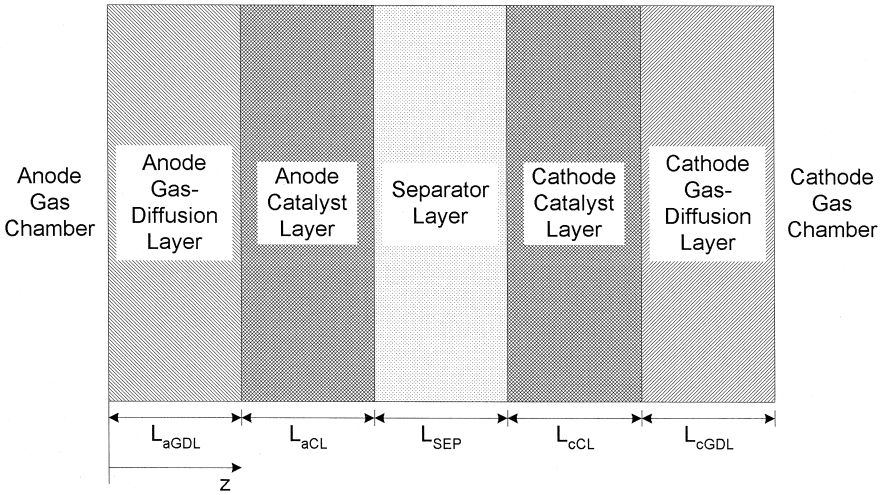

Fig. 1. Schematic diagram of AFC single cell.

shown in Fig. 1. In the gas-diffusion layers, it is assumed that the layers are electrically conductive and no liquid phase exists, since the major role of the layer is to prevent a leakage of electrolyte in general. On the other hand, in the separator layer, it is assumed that the layer is only ionically conductive, i.e., electrically non-conductive, and no gas phase exists in the layer.

The gaseous hydrogen supplied to the anode gas chamber diffuses across the anode gas-diffusion layer and the anode catalyst layer through macropores formed by PTFE and the inter-particle space. The hydrogen consequently dissolves in the electrolyte in the anode catalyst layer. After the dissolved hydrogen diffuses through the electrolyte film covering the catalyst surface of the anode, it reacts on the catalyst surface electrochemically with hydroxide ions which have moved through the micropores formed within the catalyst particle, i.e.,

$$H_2 + 2OH^- \rightarrow 2H_2O + 2e^- \quad (1)$$

The electrons generated by the above reaction move across the anode catalyst layer and the anode gas-diffusion layer toward the anode current-collector. The electrons which reach the current-collector leave the cell for the cathode.

Similarly, the gaseous oxygen supplied to the cathode gas chamber, after passing through the same process as the hydrogen, reacts electrochemically with water in the cathode catalyst layer, as follows:

$$O_2 + 2H_2O + 4e^- \rightarrow 4OH^- \quad (2)$$

After the hydroxide ions generated by reaction (2) pass through the micropore of the cathode catalyst layer, the ion moves across the separator to the anode catalyst layer.

According to reactions (1) and (2), the overall reaction in the AFC is given by:

$$H_2 + \frac{1}{2}O_2 \rightarrow H_2O \quad (3)$$

Each layer of the cell is assumed to be a homogeneous continuum. This assumption is based on the macroscopic model of Newman and Tiedemann [5]. It is also assumed that the micropores are occupied only by liquid phase and the macropores only by gas phase. Hence, in this study, the microporosity denotes the volume fraction of the liquid phase in a layer whereas the macroporosity denotes that of the gas phase.

3. Mathematical modelling

3.1. Governing equations

3.1.1. General equations

The equation of continuity for species i can be written for a porous medium in the general form:

$$\frac{\partial \varepsilon C_i}{\partial t} = -\nabla N_i + R_i^{\mathrm{p}} + R_i^{\mathrm{e}} \quad (4)$$

where: ε is porosity; t is time; C_i and N_i refer to the concentration and molar flux of species i, respectively; R_i^{p} and R_i^{e} indicate the mass transfer rate across a phase boundary and electrochemical reaction rate of species i per unit volume of the electrode, respectively.

The flux expression, N_i, depends on whether species i exists within a gas or a liquid phase. In the gas phase, the Stefan–Maxwell equation can be employed:

$$\nabla y_i = \sum_j \frac{RT}{P\mathscr{D}_{ij}^{\mathrm{g}}}\left(y_i N_j^{\mathrm{g}} - y_j N_i^{\mathrm{g}}\right) \quad (5)$$

where: R is the gas constant; T is the temperature; P is the total pressure; superscript g denotes the gas phase; y_i and $\mathscr{D}_{ij}^{\mathrm{g}}$ refer to the gas phase mole fraction of species i and the gas phase effective diffusivity of species i in j, respectively.

In the liquid phase, the Nernst–Plank equation can be employed:

$$N_i^{\mathrm{l}} = -\mathscr{D}_i^{\mathrm{l}}\nabla C_i - z_i \varkappa_i F C_i \nabla \Phi - C_i v \quad (6)$$

where: F is the Faraday constant; Φ is the solution phase potential; $\mathscr{D}_i^{\mathrm{l}}$, z_i and ω_i indicate liquid phase effective diffusivity, charge number and effective mobility of species i, respectively. The superscript l refers to the liquid phase. The effective diffusivity $\mathscr{D}_i$ is related to the free stream diffusivity D_i, porosity ε and tortuosity τ as follows:

$$\mathscr{D}_i = \frac{\varepsilon D_i}{\tau} \tag{7}$$

Similarly, the effective mobility ω_i can be expressed as:

$$\omega_i = \frac{\varepsilon^{\mathrm{l}} u_i}{\tau^{\mathrm{l}}} \tag{8}$$

If an equilibrium is assumed at the gas-electrolyte interface, the mass-transfer rate across the phase boundary R_i^{p}, can be described approximately as follows:

$$R_i^{\mathrm{p}} = -a^{\mathrm{g}} D_i^{\mathrm{l}} \left(\frac{H_i P_i - C_i}{\delta} \right) \tag{9}$$

where: a^{g} is the specific area of the gas-electrolyte interface; H_i is the Henry's law constant of species i; δ is the thickness of the electrolyte film. The minus sign before a^{g} indicates that species i goes out across a phase boundary from the current phase. Hence, when species i come into the current phase from the other, this sign is converted into plus.

The electrochemical reaction rate per unit volume R_i^{e}, can be represented by:

$$R_i^{\mathrm{e}} = -\frac{s_i a^{\mathrm{l}} i}{nF} \tag{10}$$

where a^{l} is the specific area of the catalyst-electrolyte interface, and n is the number of electrons transferred. The stoichiometric coefficient of species i, s_i, is given by expressing an electrochemical reaction in the form:

$$\sum_i s_i M_i^{z_i} \rightarrow n e^- \tag{11}$$

The local current density i is described by the Butler–Volmer electrochemical reaction rate expression:

$$i = i_0 \left[\prod_i \left(\frac{C_i}{C_i^{\mathrm{r}}} \right)^{q_i} \exp\left(\frac{\alpha_{\mathrm{a}} F \eta}{RT} \right) - \prod_j \left(\frac{C_j}{C_j^{\mathrm{r}}} \right)^{q_j} \exp\left(-\frac{\alpha_{\mathrm{c}} F \eta}{RT} \right) \right] \tag{12}$$

where: i_0 is the exchange current density; C_i^{r} is the concentration of species i at a reference condition, q_i is the reaction order of species i; α_{a} and α_{c} are the apparent anodic and cathodic transfer coefficient, respectively. The local overpotential η is given by:

$$\eta = E - \Phi - U \tag{13}$$

where: E is the electrical potential at an electrically conductive solid phase; U is the theoretical open-circuit potential at a given concentrations. U is given by:

$$U = U^{\theta} - \frac{RT}{nF} \sum_i s_i \ln\left(\frac{C_i}{C_i^{\theta}} \right) \tag{14}$$

where U^{θ} is the theoretical open-circuit potential evaluated at standard concentrations C_i^{θ} and temperature T.

These general equations presented above will be employed to describe the respective layers.

3.1.2. Gas-diffusion layers

All of the water which is electrochemically produced in Obiter Fuel Cells is eliminated in the form of vapour from the anode by circulated hydrogen [6]. Hence:

$$N_{\mathrm{H}}^{\mathrm{g}} = -N_{\mathrm{w}}^{\mathrm{g}} \tag{15}$$

By contrast, oxygen is not circulated at the cathode side [6] and, thus, there is no elimination of water from this electrode. Therefore, at the cathode

$$N_{\mathrm{w}}^{\mathrm{g}} = 0 \tag{16}$$

If Eqs. (15) and (16) are respectively inserted into the Stefan–Maxwell equation, the gaseous hydrogen and oxygen molar flux expression at each gas-diffusion layer can be obtained as follows:

$$N_{\mathrm{H}}^{\mathrm{g}} = -\frac{P_{\mathrm{a}} \mathscr{D}_{\mathrm{Hw}}^{\mathrm{g}}}{RT} \frac{\nabla P_{\mathrm{H}}}{P_{\mathrm{w}}^{\mathrm{a}} + P_{\mathrm{H}}} \tag{17}$$

$$N_{\mathrm{O}}^{\mathrm{g}} = -\frac{P_{\mathrm{c}} \mathscr{D}_{\mathrm{Ow}}^{\mathrm{g}}}{RT} \frac{\nabla P_{\mathrm{O}}}{P_{\mathrm{w}}^{\mathrm{c}}} \tag{18}$$

where P_{a} and P_{c} are the total pressure of the anode and the cathode gas-diffusion layers, respectively. P_{H}, P_{O} and P_{w} refer to the partial pressure of hydrogen, oxygen and water vapour, respectively. The total pressures within each gas-diffusion layer are associated with the reactant gases and P_{w} as follows:

$$P_{\mathrm{a}} = P_{\mathrm{H}} + P_{\mathrm{w}}^{\mathrm{a}} \tag{19}$$

$$P_{\mathrm{c}} = P_{\mathrm{O}} + P_{\mathrm{w}}^{\mathrm{c}} \tag{20}$$

Since there is neither mass transfer across a phase boundary nor electrochemical reactions at the gas-diffusion layers, R_i^{p} and R_i^{e} are zero in these layers. Thus, inserting

Eqs. (17) and (18) into continuity equation, respectively, gives expressions for the gaseous hydrogen and oxygen at the steady state, as follows.

$$\nabla\left(\frac{P_a}{P_w^a + P_H}\nabla P_H\right) = 0 \tag{21}$$

$$\nabla\left(\frac{P_c}{P_w^c}\nabla P_O\right) = 0 \tag{22}$$

In a porous electrically conductive medium such as a gas-diffusion layer, the ohmic drop can be described by Ohm's law.

$$\nabla E = -\frac{I}{\sigma} \tag{23}$$

where E is the electrical potential of the electrode, I is the current density of the single cell. The effective electrical conductivity, σ, is related to the bulk electrical conductivity, κ, the volume fraction of electrically conductive solid phase, ε^s, and the tortuosity of the phase, τ^s, by:

$$\sigma = \frac{\varepsilon^s \kappa}{\tau^s} \tag{24}$$

ε^s is associated with ε^g, ε^l and the volume fraction of PTFE, ε^{TF}, by:

$$\varepsilon^g + \varepsilon^l + \varepsilon^s + \varepsilon^{TF} = 1 \tag{25}$$

Since no electrochemical reactions exist in the gas-diffusion layers, I is constant. By differentiating Eq. (23), the ohmic drop within the anode and cathode gas-diffusion layers can be expressed as:

$$\nabla^2 E_a = 0 \tag{26}$$

$$\nabla^2 E_c = 0 \tag{27}$$

In summary, there are three governing equations in the anode gas-diffusion layer, namely, Eqs. (19), (21) and (26). Similarly, the governing equations for the cathode gas-diffusion layer are given by Eqs. (20), (22) and (27).

3.1.3. Catalyst layers

There are no electrochemical reactions in the gas phase of the catalyst layers, while dissolution of the reactant gases occurs in the electrolyte. The same gaseous molar flux expressions as those for the gas-diffusion layers can be employed to each catalyst layer. For gaseous hydrogen and oxygen, if these facts are applied to the continuity equation for each catalyst layer at steady state, the following equations can be obtained.

$$\nabla\left(\frac{\mathscr{D}_{Hw}^g}{RT}\nabla P_H\right) - a_a^g D_H^l\left(\frac{H_H P_H - C_H}{\delta_a}\right) = 0 \tag{28}$$

$$\nabla\left(\frac{\mathscr{D}_{Ow}^g}{RT}\frac{P_w^c + P_O}{P_w^c}\nabla P_O\right) - a_c^g D_O^l\left(\frac{H_O P_O - C_O}{\delta_c}\right) = 0 \tag{29}$$

If an equilibrium is assumed at the gas-electrolyte interface for water, then the partial pressure of water vapour can be related to the electrolyte concentration C_e, by [7]:

$$P_w = a_w + b_w C_e \tag{30}$$

where a_w and b_w, refer to the vapour pressure of pure water.

In the liquid phase, the molar expressions for the dissolved reactant gases can be written by using the Nernst–Plank equation. Since the dissolved gases do not have any charge, the second term on the right hand side of Eq. (6) vanishes. The dissolution of reactant gases occurs across the gas-electrolyte interface into the electrolyte, and then the gases react electrochemically at the catalyst-electrolyte interface. From these facts, the following equations are obtained at steady state, for anode and cathode catalyst layers.

$$\nabla\left(\mathscr{D}_H^l \nabla C_H\right) - \nabla\left(\upsilon \blacksquare C_H\right) + a_a^g D_H^l\left(\frac{H_H P_H - C_H}{\delta_a}\right) - \frac{s_H a_a^l i_a}{n_a F} = 0 \tag{31}$$

$$\nabla\left(\mathscr{D}_O^l \nabla C_O\right) - \nabla\left(\upsilon \blacksquare C_O\right) + a_c^g D_O^l\left(\frac{H_O P_O - C_O}{\delta_c}\right) - \frac{s_O a_c^l i_c}{n_c F} = 0 \tag{32}$$

The local current density at the anode i_a Eq. (31) is described by applying the Butler–Volmer equation to the hydrogen oxidation reaction, i.e.,

$$i_a = i_o^a\left[\left(\frac{C_H}{C_H^r}\right)^{q_H}\left(\frac{C_e}{C_e^r}\right)^{q_e^a}\exp\left(\frac{\alpha_a^a F\eta_a}{RT}\right) - \left(\frac{C_w}{C_w^r}\right)^{q_w^a}\exp\left(-\frac{\alpha_c^a F\eta_a}{RT}\right)\right] \tag{33}$$

Similarly, i_c Eq. (32) is given by:

$$i_c = i_o^c\left[\left(\frac{C_e}{C_e^r}\right)^{q_e^c}\exp\left(\frac{\alpha_a^c F\eta_c}{RT}\right) - \left(\frac{C_O}{C_O^r}\right)^{q_O}\left(\frac{C_w}{C_w^r}\right)^{q_w^c}\exp\left(-\frac{\alpha_c^c F\eta_c}{RT}\right)\right] \tag{34}$$

If the concentrations of dissolved hydrogen and oxygen are neglected, the concentration of water in the electrolyte solution can be obtained from the following relationship.

$$C_e\bar{V}_e + C_w\bar{V}_w = 1 \tag{35}$$

The local overpotential of the anode η_a and that of the cathode η_c is given, respectively, by:

$$\eta_a = E_a - \Phi - U_a \tag{36}$$

$$\eta_c = E_c - \Phi - U_c \tag{37}$$

The open-circuit potential U can be obtained via the Nernst equation. Thus, for the hydrogen oxidation reaction:

$$U_a = U_a^\theta - \frac{RT}{n_a F}\ln\left[\left(\frac{C_H}{C_H^\theta}\right)^{s_H}\left(\frac{C_e}{C_e^\theta}\right)^{s_e^a}\left(\frac{C_w}{C_w^\theta}\right)^{s_w^a}\right] \tag{38}$$

Similarly, for the oxygen reduction reaction

$$U_c = U_c^\theta - \frac{RT}{n_c F}\ln\left[\left(\frac{C_O}{C_O^\theta}\right)^{s_O}\left(\frac{C_e}{C_e^\theta}\right)^{s_e^c}\left(\frac{C_w}{C_w^\theta}\right)^{s_w^c}\right] \tag{39}$$

In Eqs. (38) and (39), the standard open-circuit potential of the anode U_a^θ and that of the cathode U_c^θ are -0.87398 V vs. SHE and 0.30859 V vs. SHE at 80°C, respectively.

In KOH solution, the ions are K^+ and OH^-. For the ions, there is no dissolution across a phase boundary. Also, K^+ ions do not react electrochemically. Thus, by using continuity at steady state, Nernst–Plank and Butler–Volmer equations, for the anode:

$$\nabla\left(\mathscr{D}_+^l\nabla C_+\right) + z_+F\nabla\left(\kappa_+C_+\nabla\Phi\right) - \nabla\left(v^\blacksquare C_+\right) = 0 \tag{40}$$

$$\nabla\left(\mathscr{D}_-^l\nabla C_-\right) + z_-F\nabla\left(\kappa_-C_-\nabla\Phi\right) - \nabla\left(v^\blacksquare C_-\right) - \frac{s_-^a a_a^l i_a}{n_a F} = 0 \tag{41}$$

According to electroneutrality:

$$C_e = C_+ = C_- \tag{42}$$

Hence, by using Eq. (42), Eqs. (40) and (41) are converted to

$$\nabla\left(\mathscr{D}_+^l\nabla C_e\right) + z_+F\nabla\left(\kappa_+C_e\nabla\Phi\right) - \nabla\left(v^\blacksquare C_e\right) = 0 \tag{43}$$

$$\nabla\left(\mathscr{D}_-^l\nabla C_e\right) + z_-F\nabla\left(\kappa_-C_e\nabla\Phi\right) - \nabla\left(v^\blacksquare C_e\right) - \frac{s_-^a a_a^l i_a}{n_a F} = 0 \tag{44}$$

Similarly, for the cathode:

$$\nabla\left(\mathscr{D}_+^l\nabla C_e\right) + z_+F\nabla\left(\kappa_+C_e\nabla\Phi\right) - \nabla\left(v^\blacksquare C_e\right) = 0 \tag{45}$$

$$\nabla\left(\mathscr{D}_-^l\nabla C_e\right) + z_-F\nabla\left(\kappa_-C_e\nabla\Phi\right) - \nabla\left(v^\blacksquare C_e\right) - \frac{s_-^c a_c^l i_c}{n_c F} = 0 \tag{46}$$

As shown in the Nernst–Planck equation, convection has to be taken into account in order to describe the molar flux in the liquid phase. First, if the partial molar volume $\bar{V}_i$ is multiplied by the continuity equation, then:

$$\bar{V}_i\frac{\partial\varepsilon^l C_i}{\partial t} = \bar{V}_i\left(-\nabla N_i + R_i^p + R_i^e\right) \tag{47}$$

This equation is applied to all species within the electrolyte of the anode catalyst layer and if these equations are summed, then:

$$\begin{aligned}\frac{\partial\varepsilon_{aCL}^l\left(C_H\bar{V}_H + C_+\bar{V}_+ + C_-\bar{V}_- + C_w\bar{V}_w\right)}{\partial t} &= -\nabla\left(N_H\bar{V}_H + N_+\bar{V}_+ + N_-\bar{V}_- + N_w\bar{V}_w\right)\\ &\quad + R_H^p\bar{V}_H + R_+^p\bar{V}_+ + R_-^p\bar{V}_- + R_w^p\bar{V}_w\\ &\quad + R_H^e\bar{V}_H + R_+^e\bar{V}_+ + R_-^e\bar{V}_- + R_w^e\bar{V}_w\end{aligned} \tag{48}$$

There is no mass transfer of the ions across a phase boundary, and the K^+ ions do not participate in the electrochemical reactions. Also, for the anode catalyst layer:

$$C_H\bar{V}_H + C_+\bar{V}_+ + C_-\bar{V}_- + C_w\bar{V}_w = 1 \tag{49}$$

By definition, the volume average velocity $v^\blacksquare$ is written as [8]:

$$v^\blacksquare = \sum_i C_i v_i\bar{V}_i = \sum_i N_i^l\bar{V}_i \tag{50}$$

Thus, Eq. (48) can be reduced to:

$$\frac{\partial\varepsilon_{aCL}^l}{\partial t} = -\nabla v^\blacksquare + \left(R_H^p\bar{V}_H + R_w^p\bar{V}_w\right) + \left(R_H^e\bar{V}_H + R_-^e\bar{V}_- + R_w^e\bar{V}_w\right) \tag{51}$$

If Eq. (15) is taken into account, then:

$$R_w^p = -R_H^p = -a_a^g D_H^l\left(\frac{H_H P_H - C_H}{\delta_a}\right) \tag{52}$$

If Eqs. (9), (10) and (52) are inserted into Eq. (51), then for the anode catalyst layer at steady state:

$$\nabla v^\blacksquare = a_a^g D_H^l\left(\frac{H_H P_H - C_H}{\delta_a}\right)\left(\bar{V}_H - \bar{V}_w\right) - \left(s_H\bar{V}_H + s_-^a\bar{V}_- + s_w^a\bar{V}_w\right)\frac{a_a^l i_a}{n_a F} \tag{53}$$

Similarly, for the cathode catalyst layer at steady state:

$$\nabla v^\blacksquare = a_c^g D_O^l\left(\frac{H_O P_O - C_O}{\delta_c}\right)\bar{V}_O - \left(s_O\bar{V}_O + s_-^c\bar{V}_- + s_w^c\bar{V}_w\right)\frac{a_c^l i_c}{n_c F} \tag{54}$$

As shown in Eqs. (53) and (54), the volume average velocity is caused by the volume change before and after the reaction.

The total current density I obtained from the single cell must be equal to the integration of local current density i with respect to z in a catalyst layer. Thus:

$$I = -\int_0^{L_{CL}} a^{l} i \, dz \tag{55}$$

where L_{CL} is the thickness of the catalyst layer and z is the spatial coordinate. As in the gas-diffusion layers, the ohmic drop in electrically conductive solid phase of the catalyst layers can be described by Ohm's law. Differentiating Eq. (55) and combining with Ohm's law give expressions for the potential drop in the anode and cathode catalyst layers at steady state, as follows

$$\nabla^2 E_a = \frac{a_a^{l} i_a}{\sigma_a} \tag{56}$$

$$\nabla^2 E_c = \frac{a_c^{l} i_c}{\sigma_c} \tag{57}$$

In summary, there are seven governing equations in the anode catalyst layer, namely, Eqs. (28), (30), (31), (43), (44), (53) and (56). Similarly, the governing equations for the cathode catalyst layer are Eqs. (29), (30), (32), (45), (46), (54) and (57).

3.1.4. Separator layer

In this layer, there are no electrochemical reactions and no mass transfer across a phase boundary. There is no gas phase and no electrically conductive solid phase, also, since the layer consists of only electrolyte and electrically insulating porous solid material. Hence, five species exist in this layer, viz., dissolved hydrogen, dissolved oxygen, liquid water, and two ions, K^+ and OH^-. If the continuity equation at steady state and the Nernst–Plank equation are employed to these species except water, then:

$$\nabla\left(\mathscr{D}_H^{l} \nabla C_H\right) - \nabla\left(v^{\blacksquare} C_H\right) = 0 \tag{58}$$

$$\nabla\left(\mathscr{D}_O^{l} \nabla C_O\right) - \nabla\left(v^{\blacksquare} C_O\right) = 0 \tag{59}$$

$$\nabla\left(\mathscr{D}_+^{l} \nabla C_e\right) + z_+ F \nabla\left(\kappa_+ C_e \nabla \Phi\right) - \nabla\left(v^{\blacksquare} C_e\right) = 0 \tag{60}$$

$$\nabla\left(\mathscr{D}_-^{l} \nabla C_e\right) + z_- F \nabla\left(\kappa_- C_e \nabla \Phi\right) - \nabla\left(v^{\blacksquare} C_e\right) = 0 \tag{61}$$

As mentioned above, since neither electrochemical reactions and nor mass transfer across a phase boundary occur in this layer, then:

$$\nabla v^{\blacksquare} = 0 \tag{62}$$

In summary, there are five governing equations in the separator layer: Eqs. (58)–(62).

3.2. Boundary conditions

3.2.1. Anode gas chamber / anode gas-diffusion layer interface

At this interface, the partial pressure of water vapour P_w^a varies with the total current density I, i.e.,

$$P_w^a = f(I) \tag{63}$$

Since the anode total pressure P_a is fixed at the reference condition, the partial pressure of hydrogen P_H at this boundary is given by:

$$P_H = P_a^r - P_w^a \tag{64}$$

The anode electrical potential E_a can be arbitrarily fixed at this boundary. Hence, the value is set at zero at this boundary.

$$E_a = 0 \tag{65}$$

3.2.2. Anode gas-diffusion layer / anode catalyst layer interface

The molar flux of gaseous hydrogen is continuous at this boundary. Thus:

$$\mathscr{D}_H^{g} \nabla P_H|_{aGDL} = \mathscr{D}_H^{g} \nabla P_H|_{aCL} \tag{66}$$

Also, the anode total pressure P_a must be equal to that of the reference condition. Hence, the following condition must be satisfied at this boundary.

$$P_a^r = P_H + P_w^a \tag{67}$$

P_w^a at this boundary is determined by

$$P_w^a = a_w + b_w C_e \tag{68}$$

The total current density I is continuous at this boundary, thus:

$$\sigma \nabla E_a|_{aGDL} = \sigma \nabla E_a|_{aCL} \tag{69}$$

Since the gas-diffusion layer prevents the electrolyte from leaking, it could be assumed that the fluxes for dissolved hydrogen and the ions are zero at this boundary. Thus:

$$0 = \nabla C_H|_{aCL} \tag{70}$$

$$0 = \nabla C_e|_{aCL} \tag{71}$$

$$0 = \nabla \Phi|_{aCL} \tag{72}$$

$$v^{\blacksquare} = 0 \tag{73}$$

3.2.3. Anode catalyst layer / separator layer interface

Since the separator layer prevents the gaseous reactant gases from overflowing toward the opposite electrode, the flux of gaseous hydrogen is zero at this interface. Hence:

$$\nabla P_H|_{aCL} = 0 \tag{74}$$

P_w^a at this boundary is determined by:

$$P_w^a = a_w + b_w C_e \quad (75)$$

Since the separator is an electrical insulator, at this interface the current density in the electrically conductive phase is zero. Thus:

$$\nabla E_a|_{aCL} = 0 \quad (76)$$

The fluxes of dissolved hydrogen and the ions are continuous at this interface, thus:

$$\mathscr{D}_H^l \nabla C_H|_{aCL} = \mathscr{D}_H^l \nabla C_H|_{SEP} \quad (77)$$

$$-\mathscr{D}_+^l \nabla C_e|_{aCL} - z_+ \mu_+ F C_e \nabla \Phi|_{aCL} = -\mathscr{D}_+^l \nabla C_e|_{SEP} - z_+ \mu_+ F C_e \nabla \Phi|_{SEP} \quad (78)$$

$$-\mathscr{D}_-^l \nabla C_e|_{aCL} - z_- \mu_- F C_e \nabla \Phi|_{aCL} = -\mathscr{D}_-^l \nabla C_e|_{SEP} - z_- \mu_- F C_e \nabla \Phi|_{SEP} \quad (79)$$

Also, the gradient of volume average velocity is continuous at this boundary. Hence:

$$\nabla v^{\blacksquare}|_{aCL} = \nabla v^{\blacksquare}|_{SEP} \quad (80)$$

Unreacted dissolved oxygen within the cathode catalyst layer will diffuse towards the anode catalyst layer through the separator, and it will be quickly and completely consumed by chemical and electrochemical reactions at the anode. At this interface, thus it can be assumed that:

$$C_O = 0 \quad (81)$$

3.2.4. Separator layer / cathode catalyst layer interface

The conditions at this interface are analogous to those at the anode catalyst-layer/separator-layer interface. Hence, the same boundary conditions as at the anode catalyst layer/separator layer interface can be employed at this interface.

3.2.5. Cathode catalyst layer / cathode gas-diffusion layer interface

Since the conditions at this boundary are similar to those at the anode catalyst layer/anode gas-diffusion layer interface, the same boundary conditions are used.

3.2.6. Cathode gas-diffusion layer / cathode gas chamber interface

For P_w and P_O, the same conditions as the anode gas chamber/anode gas-diffusion layer interface can be used, as in previous cases. Since E_a at the opposite interface is set to zero, E_c at this interface can be written as:

$$E_c = E_{cell} \quad (82)$$

where E_{cell} is the cell voltage.

4. Model parameters and correlations

Because using unreasonable parameter values will lead to physically impossible results, the reasonable choice of the parameter values is as important, if not more important, than mathematical modeling. Hence, the selection has been carefully accomplished to be as realistic as possible.

4.1. Thermodynamic properties

4.1.1. Partial molar volumes and charge numbers

It is assumed that partial molar volumes are constant. The partial molar volumes of H_2O and KOH can be determined if the relation of electrolyte density with the molar concentration of the electrolyte is known, as given by Newman [9]. The density of KOH solution as a function of the molar concentration has been reported [10].

The ionic radii of the ions have been published [11]. Thus, assuming that the ions are a spheres, the volume ratio of the ions can be calculated. Then, the partial molar volumes of respective ions are determined by employing the calculated ratio to partial molar volume of KOH.

Partial molar volumes of dissolved gases in the electrolyte are not readily available. Hence, the same volume reduction ratio of water to pure water in the electrolyte has been applied to the gases. Partial molar volumes of dissolved hydrogen and oxygen in pure water have been reported [12].

The partial molar volumes and charge numbers are listed in Table 1.

Table 1
Thermodynamic and transport properties of various species in KOH solution at 80°C

	x_i^0	k_{scx} (cm^3 mol^{-1})	$\bar{V}_i$ (cm^3 mol^{-1})	z_i	t_i	λ_i^0 (cm^2 Ω^{-1} eq^{-1})
H_2	1.322×10^{-5}	129.0	25.8804			
O_2	1.440×10^{-5}	155.0	30.8574			
H_2O			17.9858			
KOH			18.8694			
K^+			5.9346	+1	0.298	163.6
OH^-			13.1822	−1	0.702	385.2

4.1.2. Solubilities of gases

It is assumed that the solubilities of the gases obey Henry's law. Hence:

$$C_i = H_i P_i \tag{83}$$

Henry's constant is given by

$$H_i = \frac{x_i}{1 - x_i}(C_w + 2C_e) \tag{84}$$

where x_i is mole fraction of gas i in the electrolyte. x_i is determined by:

$$\log\left(\frac{x_i^0}{x_i}\right) = k_{scx} C_e \tag{85}$$

where x_i^0 refers to mole fraction of gas i in pure water. x_i^0 values and the salting-out coefficient k_{scx} of hydrogen and oxygen in KOH solutions have been reported [13]. x_i^0 and k_{scx} values at 80°C are listed in Table 1.

4.2. Transport properties

By using the diffusivity equation for a binary gas mixture at low pressure [8], the gaseous diffusivities of hydrogen and oxygen in water vapour can be expressed as follows.

$$D_{Hw}^g = \frac{2.1410 \times 10^{-6} T^{2.334}}{P} \tag{86}$$

$$D_{Ow}^g = \frac{4.2076 \times 10^{-7} T^{2.334}}{P} \tag{87}$$

The diffusivities of dissolved hydrogen and oxygen in the electrolyte can be obtained by fitting an Arrenhius type equation to the experimental data of Tham et al. [14], i.e.,

$$D_H^l = 3.5166 \times 10^{-5} + 9.7553 \times 10^{-5} \exp(-225.0 C_e) \tag{88}$$

$$D_O^l = 0.9188 \times 10^{-5} + 5.3940 \times 10^{-5} \exp(-262.6 C_e) \tag{89}$$

For a 1:1 strong binary electrolyte such as KOH solution, the bulk diffusivity of electrolyte can be expressed by:

$$D_e = \frac{2 D_+ D_-}{D_+ + D_-} \tag{90}$$

The transference numbers of the cation t_+ and the anion t_- can be represented, respectively by:

$$t_+ = \frac{D_+}{D_+ + D_-} \tag{91}$$

$$t_- = \frac{D_-}{D_+ + D_-} \tag{92}$$

Hence, combining Eq. (90) with Eqs. (91) and (92) gives expressions for the diffusivities of the ions as follows.

$$D_+ = \frac{D_e}{2(1 - t_+)} \tag{93}$$

$$D_- = \frac{D_e}{2(1 - t_-)} \tag{94}$$

The bulk diffusivity of KOH solution D_e at 80°C is not readily available. Thus, D_e at 80°C at various C_e have been extrapolated from the diffusivity data at 25, 45 and 65°C given by Gubbins et al. [15], then by using a 4th-order regression with respect to $C_e^{0.5}$ the following correlation was obtained.

$$D_e = 8.2263 \times 10^{-5} - 1.2271 \times 10^{-3} C_e^{0.5} + 4.2714 \times 10^{-2} C_e - 4.6387 \times 10^{-1} C_e^{1.5} + 1.66 C_e^2 \tag{95}$$

Since the dependency of the transference number on electrolyte concentration is generally known to be very small, it could be assumed that t_i is equal to that at infinite KOH solution. The transference number in an infinite solution is given by:

$$t_i^0 = \frac{\lambda_i^0}{\lambda_+^0 + \lambda_-^0} \tag{96}$$

where λ_i^0 is the limiting ionic equivalent conductance of ion i. Hence, t_i at 80°C can be determined from Eq. (96) and the λ_i^0 values of K^+ and OH^- at 80°C. λ_i^0 values of K^+ and OH^- at 80°C have been obtained by interpolating the data reported in the literature [16], and those are listed in Table 1, with calculated t_i values.

The mobility, u_i, of an ion i can be expressed by

$$u_i = \frac{\lambda_i}{|z_i| F^2} \tag{97}$$

λ_i is given by:

$$\lambda_i = t_i \Lambda_e \tag{98}$$

where Λ_e refers to the equivalent conductance of KOH solution. Λ_e is given by:

$$\Lambda_e = \frac{\kappa_e}{C_e} \tag{99}$$

where κ_e is the ionic conductivity of KOH solution. A reliable κ_e as a function of the electrolyte concentration (wt.%) is given in the literature [16] and if the function is converted to a function of C_e, the following correlation is obtained at 80°C:

$$\kappa_e = \frac{5.6106 C_e (79.931 - 3673.9 C_e)}{(1.0016 + 37.205 C_e)^2} \tag{100}$$

Electrical conductivities of the catalyst and gas-diffusion layers are determined according to the used material.

In Obiter Fuel Cells, nickel is used as the main material of the gas-diffusion layer, platinum as that of the anode catalyst layer, and gold as that of the cathode catalyst layer [2]. The base-case values of the electrical conductivities are listed in Table 2.

4.3. Electrochemical kinetic parameters

Since the electrochemical reactions within the anode and cathode are considered to be elementary reactions, the same absolute values as the stoichiometric coefficients are used as reaction orders of the reactants and products.

Apparent anodic and cathodic transfer coefficients, α_a and α_c, in a reactions are associated with number of electron transferred as follows [17].

$$\alpha_a + \alpha_c = \frac{n}{\nu} \tag{101}$$

where ν refers to the number of times the rate-determining step occurs for the overall reaction to occur once. The value is assumed to be unity in this work, since the electrochemical reactions are considered to be elementary reactions. If one of the transfer coefficients is known, then the other can be calculated via Eq. (101). For the hydrogen oxidation reaction on platinum in KOH solution, α_a and α_c have not been reported. The Tafel slope for the hydrogen evolution reaction is reported to be about 0.12 V dec^{-1} [18]. Thus, α_a can be obtained by using Eq. (101) and the value of α_c is about 0.5 to the reported Tafel slope. For the oxygen reduction reaction on gold in KOH solution, the cathodic transfer coefficient is available [19] as a form of Tafel slope. The reported Tafel slope is 0.047 V dec^{-1} and corresponds to α_c of 1.5.

The exchange current density, i_0, is assumed to be constant. It is estimated that i_0 is the order of 10^{-4} A cm^{-2} for the hydrogen reaction [18] and about 10^{-8} for the oxygen reaction [19]. Hence, an exchange current density of 5.0×10^{-4} A cm^{-2} has been used as the anode value and 5.0×10^{-8} A cm^{-2} as the cathode value. The base-case kinetic parameters are listed in Table 3.

4.4. Structural parameters

Most values of the structural parameters for Obiter Fuel Cells are unknown, thus, assumptions must be made. The thickness of the catalyst layer L_{CL} is proportional to the catalyst loading d_{cat}. Hence,

$$L_{CL} = V_{CL}\, d_{cat} \tag{102}$$

where V_{CL} is the specific volume of the catalyst layer. When metal black is used as a catalyst, it appears that V_{CL} is of the order of 10^{-4} cm^3 mg-cat^{-1} [20]. Thus, a V_{CL} of 5.0×10^{-4} cm^3 mg-cat^{-1} has been used for both catalyst layers. In Obiter Fuel Cells, the catalyst loading for the anode is 10 mg-cat cm^{-2} and for cathode 20 mg-cat cm^{-2} [21]. Hence, L_{CL} is 0.05 mm for the anode and 0.10 mm for the cathode.

By assuming perfect wetting of the whole catalyst surface, the specific catalyst–electrolyte interface area a^l can be calculated from:

$$a^l = \frac{A_{BET}}{V_{CL}} \tag{103}$$

where A_{BET} refers to the BET surface area of the catalyst. The BET surface area of the cathode catalyst of Obiter Fuel Cells is 12.0 m^2 g^{-1} [22]. Hence, if it is assumed that the BET surfaces of the catalysts of both electrodes are equal, since the same type of metal black electrocatalysts are used for both electrodes in Obiter Fuel Cells, the a^l of both catalyst layers is 2.4×10^5 cm^2 cm^{-3}.

Table 2
Base-case electrical conductivities of electrode layers

	Main material	κ (S cm^{-1})
Gas-diffusion layers	Ni	1.0112×10^5
Anode catalyst layer	Pt	0.9434×10^5
Cathode catalyst layer	Au	4.8780×10^5

Table 3
Base-case electrochemical kinetic parameters of anode and cathode

Parameter	Anode	Cathode
n	2	4
s_H	1	
s_O		−1
s_w	−2	−2
s_-	2	4
q_H	1	
q_O		1
q_w	2	2
q_-	2	4
α_a	1.5	2.5
α_c	0.5	1.5
i_0 (A cm^{-2})	5.0×10^{-4}	5.0×10^{-8}

Table 4
Base-case values of structural parameters and thicknesses of electrode layers

Parameter (unit)	Gas-diffusion layer	Catalyst layer	Separator layer
L (cm)	0.025	0.005 (anode) 0.010 (cathode)	0.005
ε^g	0.7	0.1	
ε^l		0.6	0.8
ε^s	0.2	0.2	
τ	1.2	1.2	1.0
a^g (cm^{-1})		7.0×10^3	
a^l (cm^{-1})		2.4×10^5	
δ (cm)		5.0×10^{-5}	

Table 5
Base-case operating conditions

Parameter	Value (unit)
C_e^r	7.0 (M)
T	80 (°C)
P_a^r	4.1 (atm)
P_c^r	4.1 (atm)

Specific gas–electrolyte interface areas a^g of the catalyst layers of Obiter Fuel Cells have not been reported, thus a value of 7.0×10^3 cm^2 cm^{-3} has been assumed for both catalyst layers. The value seems to be reasonable, because several researchers have used a value of 10^3 cm^2 cm^{-3} for a^g [7,23,24], which corresponds to the limiting current density of several A cm^{-2}. The thickness of the electrolyte film δ has been reported to be about 10^{-1} μm [7,23,24]. Thus, 0.5 μm was assumed for both catalyst layers.

The thickness of the separator layer has been reported as 50 μm [21]. Although, the porosity of the layer has not been disclosed, it has been assumed to be 0.8.

The base-case values of the structural parameters and the thicknesses used in this work are listed in Table 4.

4.5. Operating conditions

Orbiter Fuel Cells operated typically at 80°C and a gas pressure of 4.1 atm with 7 M KOH solution. Hence, these have been considered as the base-case operating conditions in this study. The operating condition is listed in Table 5.

During prediction of operating pressure effects, the total pressures of the anode and the cathode gas-diffusion layers were set at the operating pressure to avoid overflow of the gases across the separator layer.

5. Method of solution

The model developed in this study consists of 11 variables, 25 governing equations and 38 internal and outer boundary conditions. The model equations are highly coupled and non-linear and thus a numerical solution is required. The governing equations and boundary conditions have been discretized through the use of second-order and first-order finite difference schemes, respectively. The resulting finite difference approximations have a banded matrix structure and have been solved by use of the BAND algorithm developed by Newman [25].

6. Results and discussion

6.1. Comparison of model with experimental data

A comparison of the model prediction with some experimental data is given in Fig. 2. The open circles indicate the experimental polarization of the Orbiter Fuel Cell [26] which is considered as the base-case model in this study. The open squares indicate the experimental data of BZA4 system of Siemens [27]. The solid lines are the model predictions. In order to predict the polarization of BZA4, another parameter set was used and is listed in Table 6. Some unknown values of the parameters for BZA4 were adjusted within a reasonable range in order to fit the model prediction to the polarization data, and the values of some parameters were assumed to be equal to that of the base-case (Table 6). Good agreement with the experimental data, as shown in Fig. 2, suggests that the present model provides a good prediction of the polarization characteristics of AFCs.

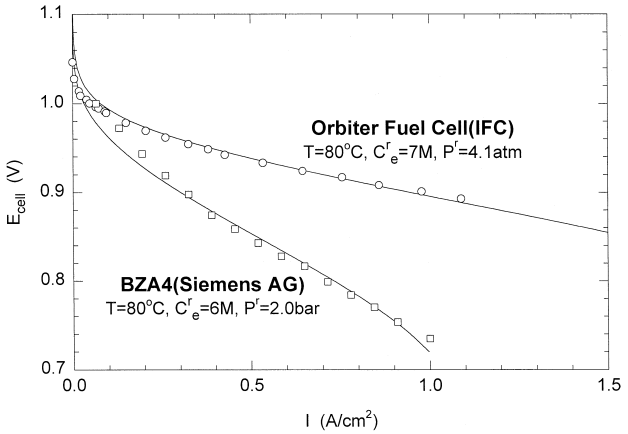

Fig. 2. Comparison of model predictions with experimental data. Solid lines are model predictions and open dots are experimental data.

6.2. Polarization curve and Tafel plot for base-case

The polarization curve for the base-case displays a typical shape and includes all types of polarization, (activation, ohmic and concentration polarization) in fuel cells is given in Fig. 3. The single cell has an open-circuit voltage of 1.136 V, a limiting current density I_L of about 2.2 A cm^{-2}, and a slope in the linear region (ohmic polarization

Table 6
Parameter values used for BZA4 (Siemens)

	Parameter (unit)	Value
Operating condition	C_e^r (M)	6.0
	P_a^r (bar)	2.0
	P_c^r (bar)	2.0
Catalyst layer	L_{CL} (cm)	0.06 (anode)
		0.03 (cathode)
	ε_{CL}^l	0.1[a]
	i_o (A cm^{-2})	1.5×10^{-4} (anode)[a]
		1.5×10^{-8} (cathode)[a]
	κ_{CL} (S cm^{-1})	1.0112×10^5 (anode, Ni)
		5.2477×10^5 (cathode, Ag)
Separator layer	L_{SEP} (cm)	0.05[a]

[a] Indicates assumed value.

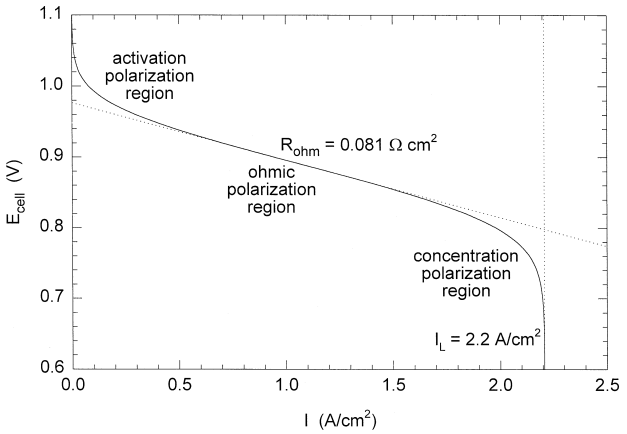

Fig. 3. Predicted polarization curve for base-case.

region) R_{ohm} of 0.081 Ω cm^2. As shown in Fig. 3, the range of the cell voltage E_{cell} from 0.7 to 0.6 V corresponds to I_L. Additionally, the maximum power density of the cell is about 1.63 W cm^{-2} at an E_{cell} of 0.77 V.

The Tafel plot for the base-case is shown in Fig. 4. The Tafel slope is 47.3 mV dec^{-1} and the apparent exchange current density is 1.19×10^{-4} A cm^{-2}. According to our analysis, it is found that these values corresponded to those of the cathode. Hence, it seems that electrochemical kinetic parameters such as the exchange current density and the Tafel slope obtained from a Tafel plot of an AFC single cell are those of the cathode. Conversely, it appears that electrochemical kinetic parameters of the anode cannot be determined from the Tafel plot of an AFC single cell.

6.3. Distribution of the variables

The distribution of the partial pressure of gaseous hydrogen P_H as a function of E_{cell} is given in Fig. 5. It is found that decreasing E_{cell} or increasing I results in less uniform distribution of P_H. The pressure drop throughout

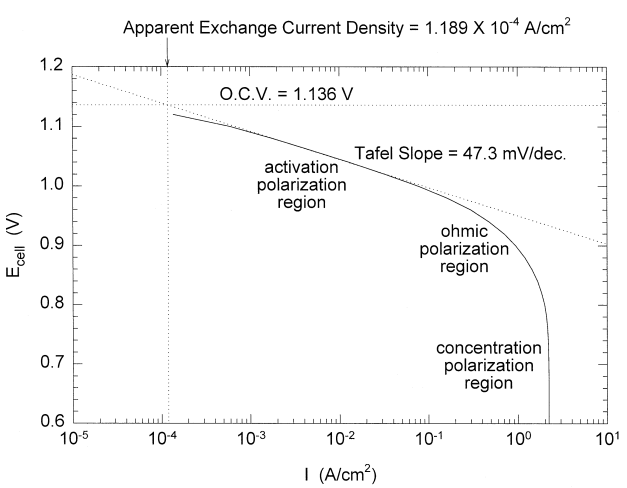

Fig. 4. Predicted Tafel plot for base-case.

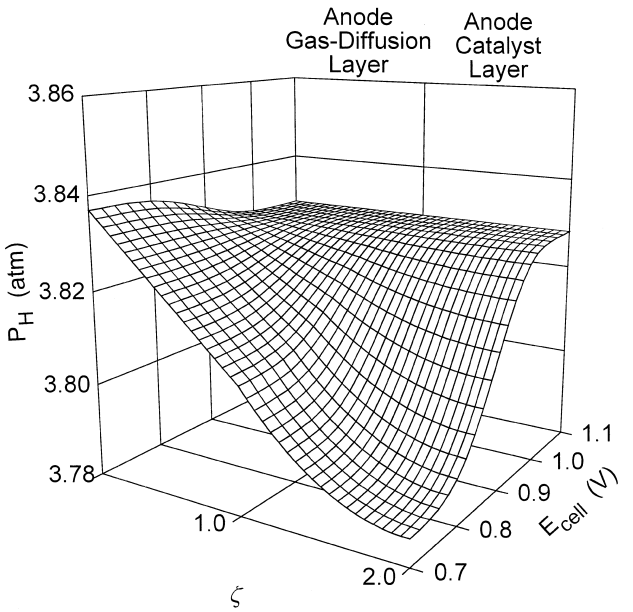

Fig. 5. Profile of partial pressure of hydrogen in anode as a function of cell voltage.

the gas-diffusion layer and the catalyst layer of the anode, however, is very small, i.e., ~0.05 atm, even at I_L. Thus, the gas-phase diffusional resistance of gaseous hydrogen can be considered to be insignificant. Additionally, the fact that P_H converges to a constant value at E_{cell} corresponding to I_L implies that the gas phase diffusion of hydrogen is not the rate-determining step at I_L.

The distribution of the partial pressure of gaseous oxygen P_O is presented in Fig. 6. The behaviour is similar to that of P_H. Note that, the pressure drop across the layers is

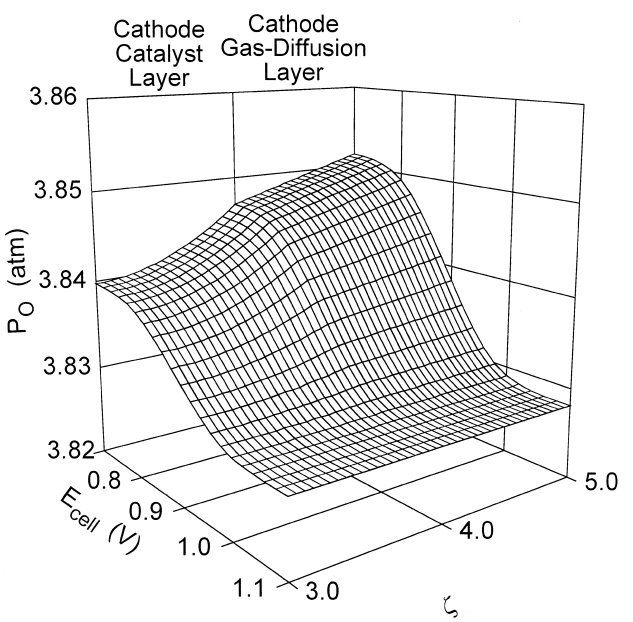

Fig. 6. Profile of partial pressure of oxygen in cathode as a function of cell voltage.

smaller than that of P_H. Two reasons that may be responsible for this phenomenon are: (i) the consumption rate of oxygen is slower than that of hydrogen, thus a smaller pressure gradient is needed for P_O at the same I; (ii) gaseous hydrogen must diffuse against the flux of anode water vapour, but, gaseous oxygen does not experience a resistance due to the flux of water vapour, since removal of water vapour was not employed at the cathode side as mentioned earlier. Also, a rise in average P_O as E_{cell} decreases is observed, see Fig. 6. This phenomenon results from a decrease of partial pressure of water vapour P_w within the cathode caused by increasing the electrolyte concentration in the cathode catalyst layer, as will be seen later (see also Eq. (30)).

As for P_H, it can be considered that gas-phase diffusion of oxygen is not a rate-determining step at I_L.

Profiles of the concentration of the dissolved hydrogen C_H and oxygen C_O are shown in Figs. 7 and 8, respectively. The profiles displays similar behaviour, the concentration decreases with decrease in E_{cell}, C_H remains constant at I_L, while C_O converges to zero. This prediction is consistent with that of Kimble and White [4] and suggest that the cathode suffers from lack of dissolved oxygen and I_L is caused by the lack of the oxygen due to a large liquid-phase diffusional resistance. Also, note that the gas-electrolyte interface area per apparent electrode area of the cathode is twice as large as that of the anode, because the thickness of the cathode catalyst layer L_{cCL} is twice as thick as that of the anode catalyst layer L_{aCL} while still having the same specific gas-electrolyte interface area a^g. Moreover, the cathode consumes less reactant gas than the anode. The fact that the lack of dissolved reactant gas occurs at the cathode suggests that cathodes in AFCs are suffer more from the lack of dissolved oxygen than anodes. In order to reduce the liquid-phase diffusional resistance of oxygen or to increase I_L, more sites for oxygen dissolution are required.

The profile of the concentration of KOH solution, C_e is given in Fig. 9. Because C_e affects most properties, such as liquid phase diffusivity, solubility and reaction rate, the

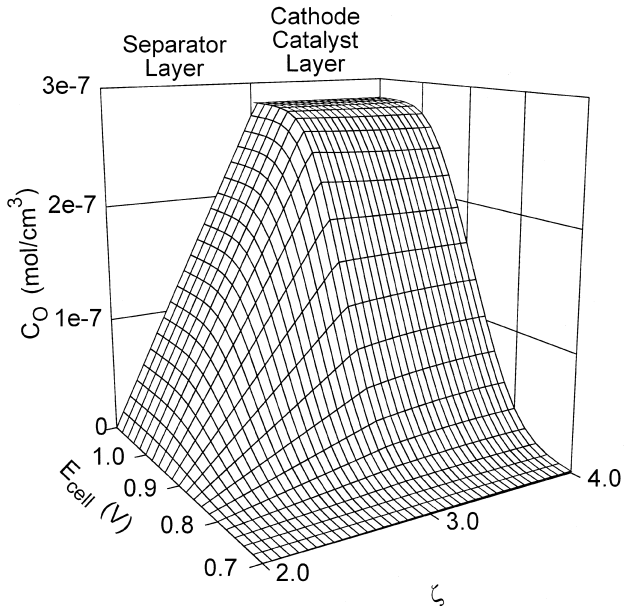

Fig. 8. Profile of concentration of dissolved oxygen in separator and cathode as a function of cell voltage.

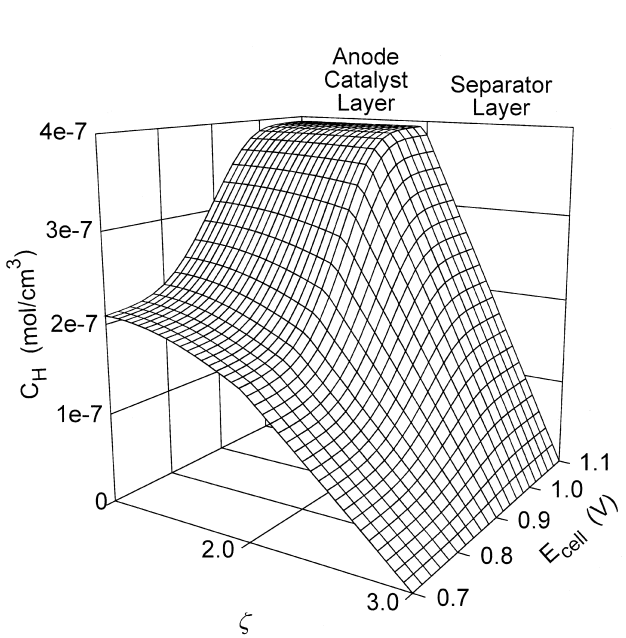

Fig. 7. Profile of concentration of dissolved hydrogen in anode and separator as a function of cell voltage.

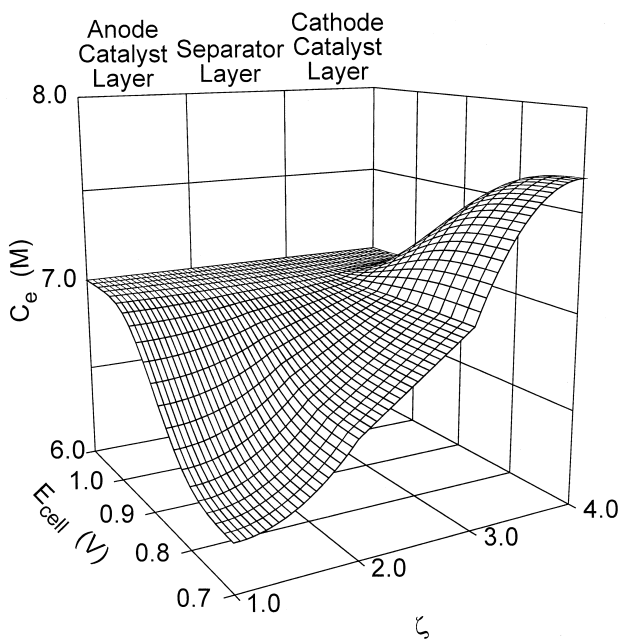

Fig. 9. Profile of electrolyte concentration in anode, separator and cathode as a function of cell voltage.

profile of C_e is very important, especially in understanding the phenomena that take place in an AFC. As shown, C_e decreases within the anode and increases within the cathode as E_{cell} decreases. If the reactions at each electrode are taken into account, this phenomenon is sufficiently predictable. Since the concentration drop across the layers is estimated to be about 1.4 M, however, the non-uniform distribution of C_e is quite serious. Therefore, it is considered that the assumption of uniform distribution of the electrolyte, which has been used in most mathematical models, is not valid, especially at high I. Hence, it can be concluded that a model which assumes uniform C_e cannot represent a high-performance electrode or single cell. The data in Fig. 9 also reveal that the lack of dissolved oxygen within the cathode is partly due to this variation in C_e. Note that, an increase in C_e leads to a decrease in gas solubility.

The solution phase potential, Φ, is shown in Fig. 10. The value of Φ at the anode is obviously higher than that at the cathode. This fact indicates that OH^- ions are attracted to the anode side, as expected. Also, as with C_e, the variation in Φ increases with decrease in E_{cell}. The variation across the separator layer corresponds to the ohmic drop between the electrodes. The ohmic drop within the separator layer is 7.6 mV at a cell voltage of 0.7 V. This value accounts for only 1.74% of the total cell polarization. Hence, the ohmic drop due to the electrolyte resistance in the base-case model appears to be insignificant.

The profiles of electrical potential at the anode E_a and the cathode E_c have been also investigated. The ohmic drop throughout each electrode was predicted to be of the order of μV, even at I_L. This is due to the high electrical conductivities of the electrode materials, as shown in Table 2. If a material that has a lower conductivity such as carbon is employed, however, the ohmic drop in the electrode becomes significant.

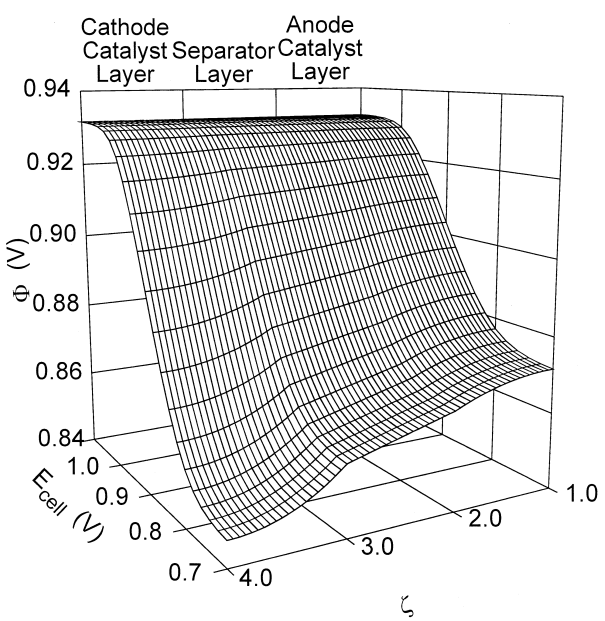

Fig. 10. Profile of solution phase potential in anode, separator and cathode as a function of cell voltage.

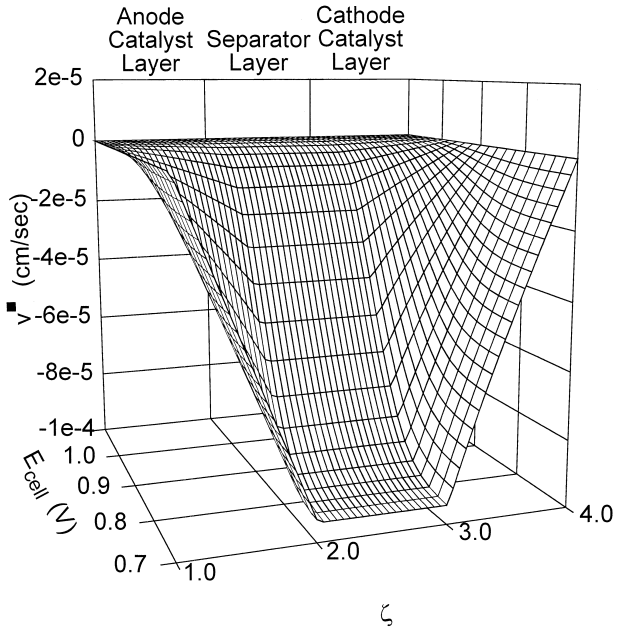

Fig. 11. Profile of volume average velocity in anode, separator and cathode as a function of cell voltage.

The distribution of the volume average velocity $v^{\blacksquare}$ is given in Fig. 11. The value of $v^{\blacksquare}$ within the separator is only -0.94 μm s^{-1}, even at I_L. Also, the minus sign in the value implies that the solution moves from the cathode to the anode, and this corresponds to the direction of OH^- flux. Thus, it can be concluded that the convection in the solution phase occurs in a direction which helps the transport of OH^-, but the magnitude of $v^{\blacksquare}$ is too small.

In order to investigate which term is important in the mass transfer of OH^-, the values of the respective terms in Nernst–Planck equation, which are classified as the diffusion, migration and convection terms, are calculated within the separator layer at $I = 1.0$ A cm^{-2}. The results are listed in Table 7. Most of the transport depends on diffusion and migration. By contrasts, the convection occupies only 2.9% of the total molar flux and thus appears to be

Table 7
Analysis of mass transfer of hydroxide ion in separator layer (at $I = 1.0$ A cm^{-2})

Term	Molar flux (mol cm^{-2} s^{-1})	Percentage (%)
Diffusion	-4.632×10^{-6}	44.7
Migration	-5.431×10^{-6}	52.4
Convection	-0.301×10^{-6}	2.9
Total	-10.364×10^{-6}	100.0

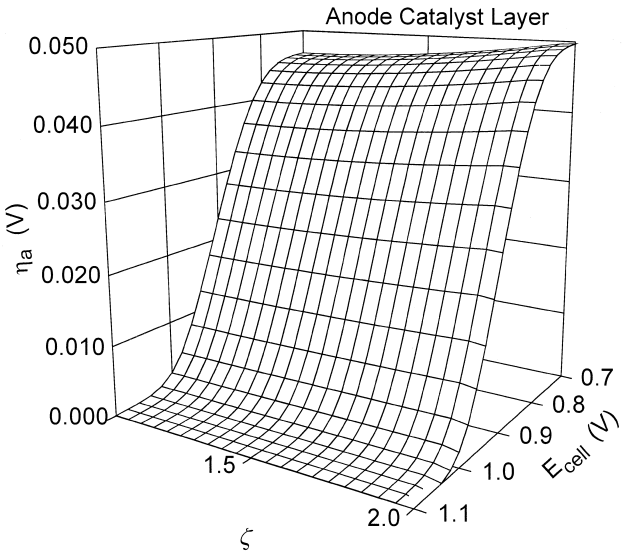

Fig. 12. Profile of anode local overpotential in anode catalyst layer as a function of cell voltage.

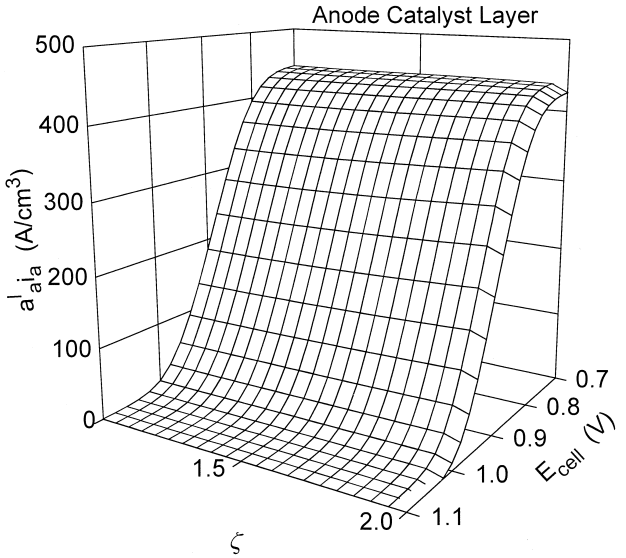

Fig. 14. Profile of apparent local current density in anode catalyst layer as a function of cell voltage.

negligible. Hence, the assumption of no convection, which has been employed in many mathematical models, seems to be valid.

The local overpotential at the anode η_a and the cathode η_c is shown in Figs. 12 and 13, respectively. η_a increases up to about 45 mV with decrease in E_{cell}. While, η_c increases up to about 300 mV. As for other fuel cells, it is confirmed that in the base-case cell most of the polarization is caused by the cathode. As is well known, this phenomenon results from the low exchange current density i_0 of the oxygen reduction reaction at low I and the lack of dissolved oxygen at high I, as shown in Fig. 8. Additionally, it is observed that η_a is constant at I_L, while η_c continuously increases, even at I_L. This implies that the limiting factor for I_L exists at the cathode. This fact is in good agreement with the analysis in Fig. 8.

The distribution of apparent local current density $a^l i$ of the anode and the cathode is shown in Figs. 14 and 15, respectively. Note that $a^l i$ means the electrochemical reaction rate. Comparison of the two sets of data shows that $a^l i$ of the anode is approximately twice as the large as that of the cathode at I_L. This phenomenon is associated with the fact that L_{cCL} is twice as large as L_{aCL}. It is also observed that the distribution of the anode $a^l i$ is relatively uniform, while that of the cathode is not. Within the cathode catalyst layer, the $a^l i$ on the separator layer side is

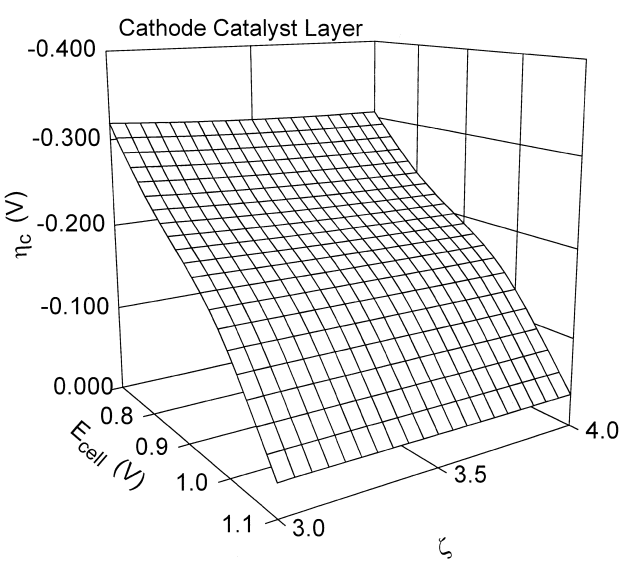

Fig. 13. Profile of cathode local overpotential in cathode catalyst layer as a function of cell voltage.

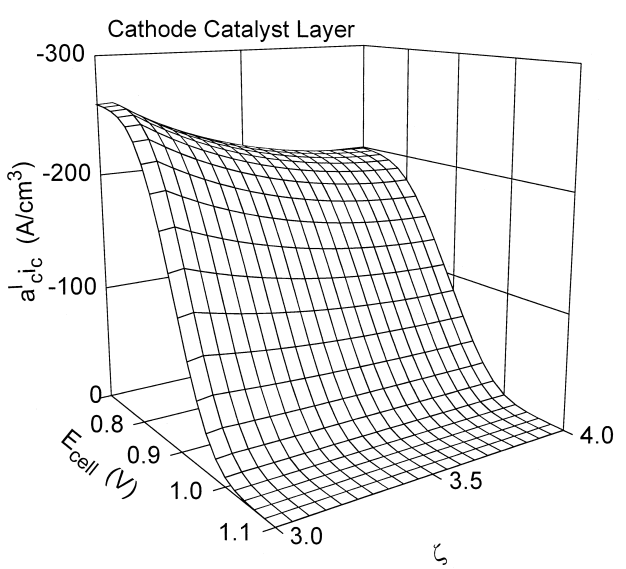

Fig. 15. Profile of apparent local current density of cathode catalyst layer as a function of cell voltage.

larger than that on the gas-diffusion layer side. This is considered to be due to the lower C_e on the separator layer side, as shown in Fig. 9. Note that, the lower C_e at the cathode is favourable for the oxygen reduction reaction.

6.4. Influence of operating condition

6.4.1. Influence of initial electrolyte concentration

Since most thermodynamic, transport and electrochemical properties of the reactants are functions of the electrolyte concentration C_e, a variation in the initial electrolyte concentration C_e^r could have a large effect on cell performance. For instance, increasing C_e decreases the gas solubility and the partial pressure of water vapour. It also enhances the hydrogen oxidation kinetics but diminishes the oxygen reduction rate as expected from Eqs. (33) and (34). Hence, the variation in C_e^r will lead to very complicated phenomena.

The influence of C_e^r on cell polarization is presented in Fig. 16. By lowering C_e^r, the performance is enhanced in the ohmic and concentration polarization region, except in the case of 1 M. On the other hand, I in the active polarization region steadily increases with the lowering of C_e^r. This behaviour can be seen clearly in Fig. 17, namely, dilution of C_e^r from 6 to 4 M dramatically increases I at low cell voltage, but dilution below 3 M reduces I to a large extent. The optimum value of C_e^r is between 3.0 and 3.5 M, except when E_{cell} is 1.0 V. These values are considerably different from the concentration between 6 and 7 M, which is commonly used in AFC systems. KOH solution with a concentration between 6 and 7 M is used due to the fact that the electrolyte has maximum ionic conductivity at this concentration [28], as shown in Fig. 18. In the later, the ionic conductivity κ_e was calculated from Eq. (100). The experimental data on the effects of C_e^r on the performance of an AFC single cell are not readily available, but it has been reported [23] that the electrolyte concentration at the highest performance of a Raney nickel hydrogen electrode is approximately 4 M. Although the different electrodes and operating pressure were used, this value is similar to that of the present study. Thus it is considered that the concentration of 6 and 7 M, which is commonly used in most AFC systems, may not be an optimum value. Simultaneously, it should be noted that low electrolyte concentration could yield some problems such as flooding of the catalyst layer or difficulty in water management due to an increase in the partial pressure of

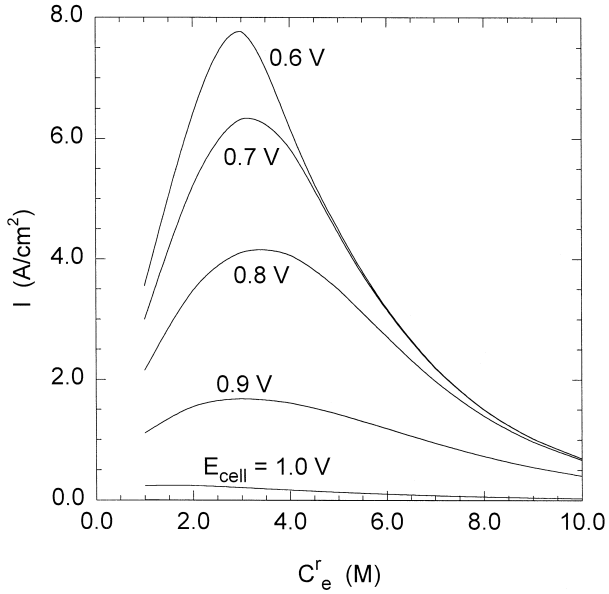

Fig. 17. Effect of initial electrolyte concentration on current density as a function of cell voltage.

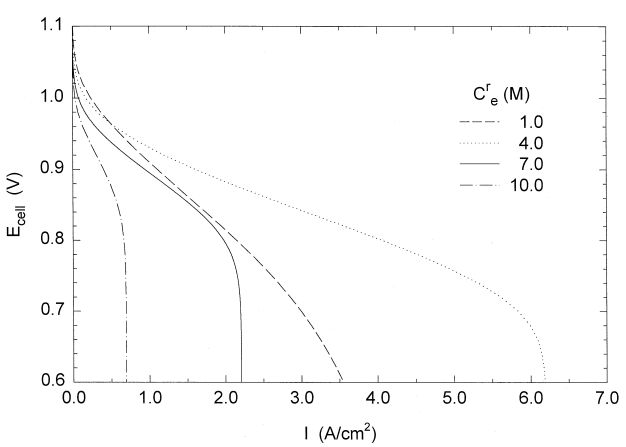

Fig. 16. Influence of initial electrolyte concentration on polarization of AFC.

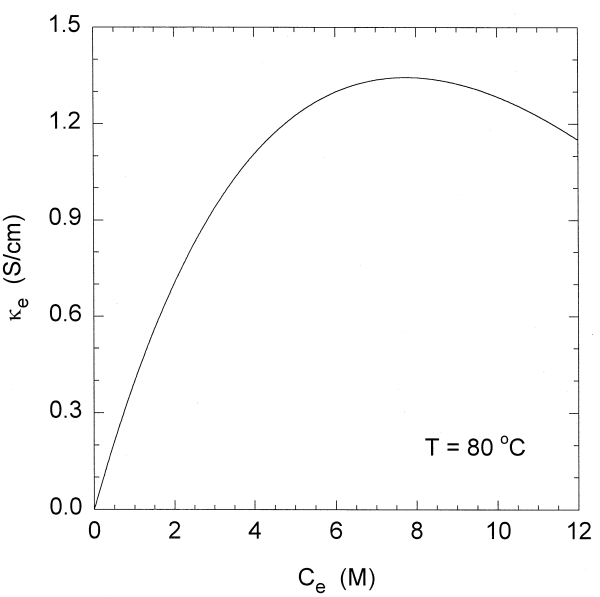

Fig. 18. Ionic conductivity of KOH solution as a function of concentration.

water vapour. These problems are, however, beyond the scope of this work.

Distinct influences of dilution C_e^r beyond 4 M on the polarization curves are an increase in the value of I_L and a reduction in the slope in the ohmic polarization region R_{ohm}. The increase of I_L is due to an increase in Henry's constant of oxygen H_O, which results in an increase in oxygen solubility $H_O P_O$ and in the liquid phase diffusivity D_i^l of oxygen but not hydrogen. Note that in the present AFC model, the rate, determining step at I_L is present in the cathode, not in the anode, as shown earlier. The solubility at a constant partial pressure and D_i^l of oxygen increase exponentially with decrease in C_e [13,14,29,30]. Thus, I_L increases exponentially with decreasing in C_e^r.

In influence of C_e^r on R_{ohm} is presented in Fig. 19. It can be seen that R_{ohm} decreases on reducing C_e^r at high concentration. The decrease in R_{ohm} in the range of 4 to 7 M, however, is not readily understandable because κ_e decreases with lowering of C_e in this range, as shown in Fig. 18.

In order to investigate whether there is a decease in the ionic resistance within the cell as C_e^r decreases in spite of the decrease in κ_e, the potential drops in the electrolyte, $\Delta\Phi$, throughout the catalyst layers and the separator layer were calculated at a current density of 1.0 A cm^{-2}. The value of $\Delta\Phi$ was 13.2 mV and 11.4 mV at 4 and 7 M, respectively. Obviously, increasing C_e^r reduces $\Delta\Phi$, as predicted in Fig. 18. Therefore, the decrease in R_{ohm} is not considered to be due to ionic resistance. Additionally, the decrease in R_{ohm} is not due to the electrical resistance in the cell since this resistance is independent of C_e.

As mentioned above, lowering C_e^r leads to an increase in I_L. This implies that a decrease in the liquid-phase diffusional resistance of the dissolved gases occurs as C_e^r decreases. The former can yield a decrease in R_{ohm}, since the diffusional resistance is known to contribute to R_{ohm} to a certain extent [31]. In Fig. 20, it can be seen that reducing C_e^r from 7 to 4 M makes the concentration of the dissolved hydrogen, C_H, and that of dissolved oxygen, C_O, about three times higher. Such large increases in C_H and C_O clearly indicate a decrease of the liquid phase diffusional resistance. Therefore, the decrease in R_{ohm} appears to be affected by a decrease in the liquid phase diffusional resistances of the dissolved gases.

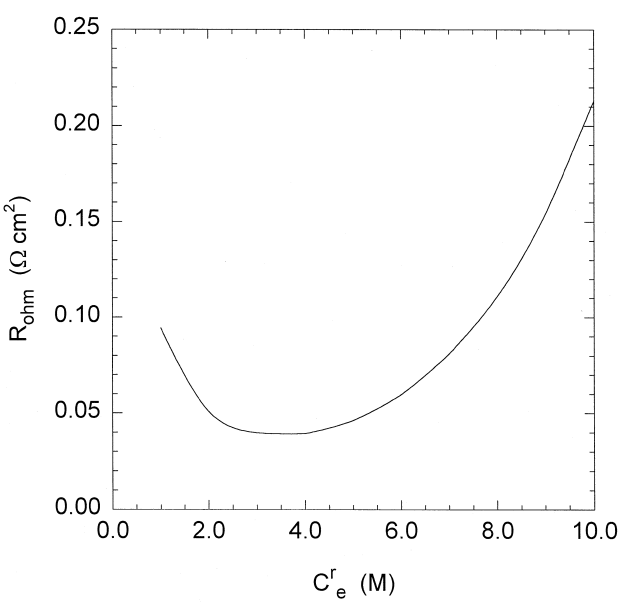

Fig. 19. Slope of ohmic polarization region as a function of electrolyte concentration.

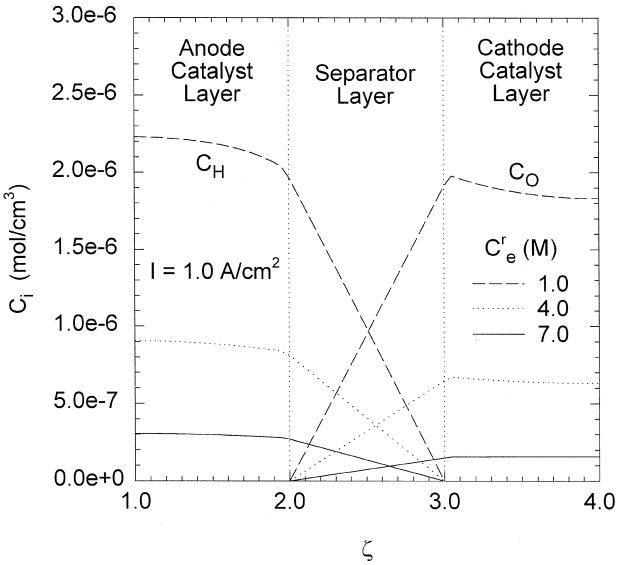

Fig. 20. Distribution of dissolved gases as a function of electrolyte concentration.

Another possible reason for the decrease in R_{ohm} is the influence of C_e on the electrochemical reaction rates, since the charge transfer resistance of the electrode is known to contribute to R_{ohm} [31]. As expected from Eqs. (1) and (2), a lowering of C_e enhances the charge-transfer rate of oxygen reduction, but decreases that of hydrogen oxidation. This fact implies that the charge-transfer resistance of the cathode decreases, and that of the anode increases, as C_e^r is diluted. For $E_{cell} = 1.0$ V in Fig. 17, it can be confirmed that the charge-transfer resistance of the cathode is reduced with lowering of C_e^r. Note that, this cell voltage corresponds to the activation polarization region where the charge-transfer resistance of the cathode is dominant. Hence, the decrease in R_{ohm} is partly due to the decrease in the charge-transfer resistance of the cathode.

Consequently, the decrease in R_{ohm} with decreasing C_e^r in the range 4 to 7 M is considered to result from the decreases in the liquid-phase diffusional resistances of the dissolved gases and from the decrease in the charge-transfer resistance of the cathode.

A decrease in the performance due to the lowering of C_e^r at below 4 M can be observed in Figs. 17 and 19, in

spite of the increase of C_H and C_O as shown in Fig. 20. Two factors can explain such a phenomenon. First, as shown in Fig. 18, diluting C_e to below 4 M diminishes κ_e. Hence, diluting C_e^r will increase the ionic resistance of the cell. According to our calculations, $\Delta\Phi$ throughout the catalyst layers and separator layer is 13.2 and 34.2 mV at C_e^r of 4 and 1 M, respectively, when I is 1.0 A cm^{-2}. Thus, the increase in the ionic resistance is considered to decrease the cell performance. The second factor to cause decrease in the performance is the use of the electrolyte with low concentration, which has an unfavourable effect on the hydrogen oxidation at the anode. The distribution of the open-circuit potential of the anode U_a and that of the cathode U_c as a function of C_e^r is shown in Fig. 21. Despite the increase in C_H and C_O with decreasing C_e^r, as shown in Fig. 20, an increase in U_a, which is unfavourable to the hydrogen oxidation, is observed in Fig. 21. If the increase of C_H and the Nernst equation of the anode Eq. (38) are taken into account, it is evident that the rise of U_a is due to the extremely low C_e^r. Hence, it seems a that lower C_e^r creates greater charge-transfer resistance of the anode, and the greater resistance contributes to the increase of R_{ohm}.

Consequently, it is concluded that the increase of R_{ohm} with the decreasing of C_e^r at below 4 M is caused by an increase in the ionic resistance, of the cell and by an increase in the charge-transfer resistance of the anode.

6.4.2. Influence of operating pressure

Polarization curves as a function of the operating gas pressure P^r as shown in Fig. 22. Increasing P^r is well known to have a positive effect on the performance of AFCs [28]. The data in Fig. 22 are consistent with this fact.

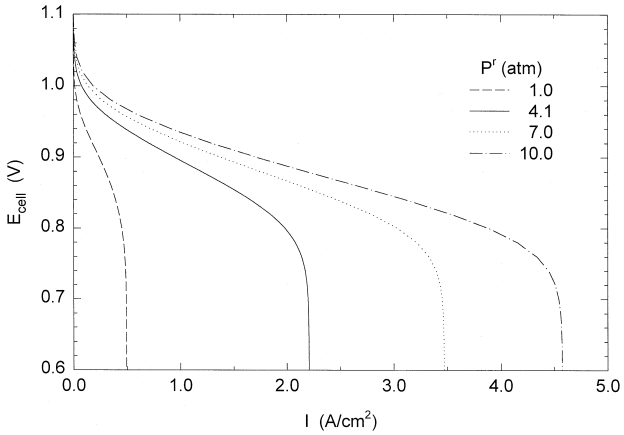

Fig. 22. Influence of operating pressure on polarization of AFC.

Increase in I in all polarization regions with increasing P^r can be observed in Fig. 22. In particular, an increase in I_L and a decrease in R_{ohm} are noticeable.

The I_L can be increased by an increase in the liquid-phase diffusivity or the solubility of the reactant gases. The solubility $H_i P_i$ is composed of Henry's constant H_i, and partial pressure of the gas P_i; H_i and P_i are functions of C_e. According to our analysis, there is no change in C_e distribution throughout the cell with increasing P^r at constant I. Thus, H_i and D_i^l of the gases remain constant with increasing P^r. Moreover, since it is assumed that these are no changes in the electrode structure which could affect I_L during the varying pressure, any influences by the structural parameter are absent. Therefore, it is concluded that the increase in I_L is caused solely by the increases of P_H and P_O due to the increasing P^r.

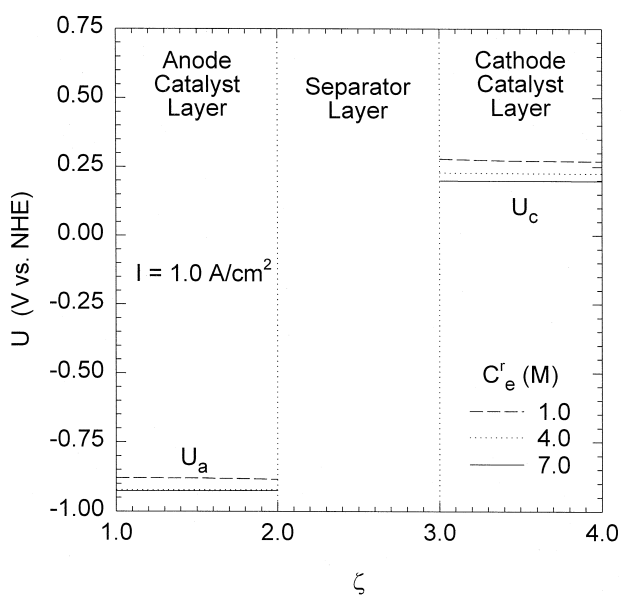

Fig. 21. Distribution of open-circuit potential as a function of electrolyte concentration.

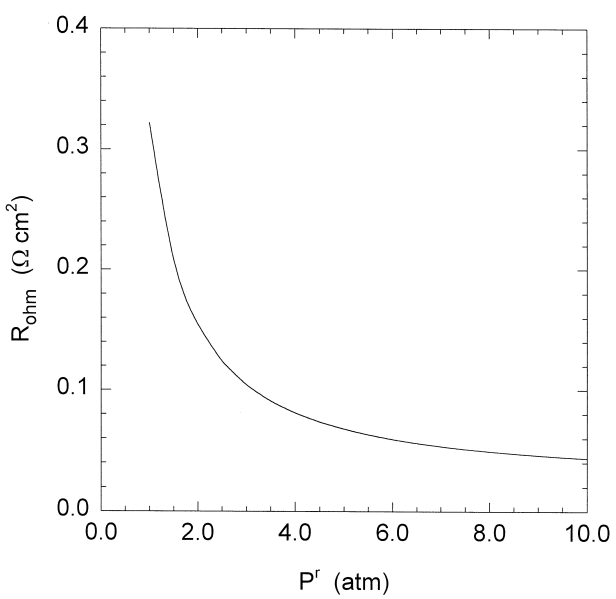

Fig. 23. Slope of ohmic polarization region as a function of operating pressure.

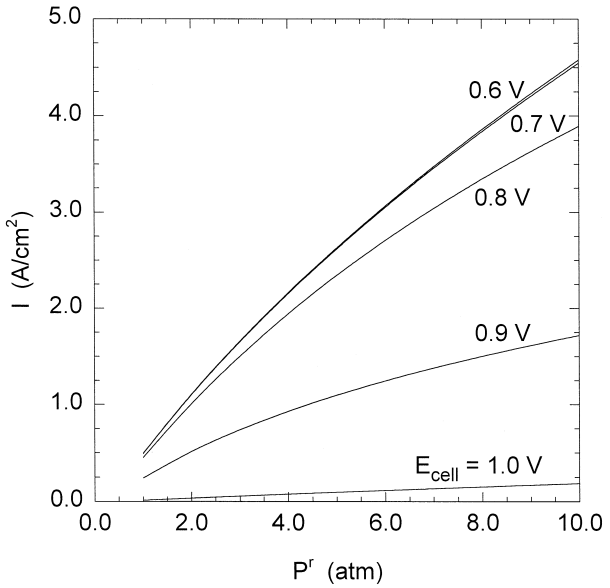

Fig. 24. Effect of operating pressure on current density as a function of cell voltage.

R_{ohm} as a function of P^r is presented in Fig. 23. At low P^r, a small increase in P^r considerably decreases R_{ohm}, while at high pressure even a large increase in P^r causes only a small variation in R_{ohm}.

As mentioned in the previous section, R_{ohm} can be affected by ionic or electrical resistance, charge-transfer resistance and liquid-phase diffusional resistance [31]. Hence, all these factors can be considered as reasons for the decrease of R_{ohm} with increasing P^r. In order to investigate the influence of the ionic resistance, $\Delta\Phi$ values throughout the catalyst layers and separator layer were calculated in the P^r range of 1 to 10 atm at constant I. According to calculation, $\Delta\Phi$ does not varied at all with varying P^r. Additionally, it should be noted that the electrical resistance is not a function of the operating pressure. Hence, neither the ionic nor the electrical resistance is not responsible for the decrease in R_{ohm} with increasing P^r. An increase in P^r allows faster charge-transfer rate, and such an effect can be confirm from the case of 1.0 V in Fig. 24. It should be also noted that R_{ohm} decreases with increase in I_L, as mentioned in the previous Section. Therefore, the decrease of R_{ohm} is considered to be caused by the decrease in the charge-transfer resistances and by the increase in the gas solubilities due to increasing P_i of the reactant gases.

7. Conclusions

An advanced mathematical model has been developed for a AFC single cell. In particular, the model describes liquid-phase convection in detail and has reliable correlations and parameter values. The model predicts well the polarization characteristics of some AFCs. It is found that the kinetic parameters obtained from the Tafel plot of the single cell are very close to that of the cathode.

From the profiles of dissolved gases as a function of the cell voltage, it is considered that the liquid-phase diffusion of dissolved oxygen is the rate-determining step at limiting current density. Cathodes in AFCs are also found to suffer more from a lack of dissolved oxygen than anodes. The non-uniformity of the spatial distribution of the KOH concentration is shown to be serious, especially at high current density.

The resistances by the gaseous diffusion of the gases, the electron conduction in the solid phase and the convection in the liquid phase are considered to be negligible, even at high current density.

Influences of the operating condition in the AFC are also investigated. It is shown that the initial electrolyte concentration has an optimum of 3.0 to 3.5 M when the cell voltage is between 0.6 and 0.9 V. The current density at 1.0 V increases steadily as the electrolyte concentration is decreased. The increase in the limiting current density with dilution of the electrolyte is found to be due to an increase in Henry's constant and the liquid-phase diffusivity of the dissolved gases. It is also considered that the major factors which affect the slope of the ohmic polarization region for an electrolyte concentration of 4 to 7 M are the charge-transfer resistance of the cathode and the liquid-phase diffusional resistance of the dissolved gases. On the other hand, in for an electrolyte concentration below 4 M, the slope is considered to be affected mainly by the charge-transfer resistance of the anode and the ionic resistance of the electrolyte.

The partial pressures of reactant gases are found to be the only cause for the increase in the limiting current density with increasing operating pressure. The decrease in the slope in the ohmic polarization region with increasing pressure is considered to be caused by an enhancement of the charge-transfer rate at both electrodes and by increases in the gas solubilities.

8. List of symbols

Italic

A_{BET}	BET surface area of catalyst (cm^2 mg-cat^{-1})
a^g	specific area of gas-electrolyte interface (cm^2 cm^{-3})
a^l	specific area of catalyst-electrolyte interface (cm^2 cm^{-3})
C_i	concentration of species i (mol cm^{-3})
D_i	free stream diffusivity of species i (cm^2 s^{-1})
$\mathscr{D}_i$	effective diffusivity of species i (cm^2 s^{-1})
d_{cat}	catalyst loading (mg-cat cm^{-2})
E	electrical potential of electrode (V)
E_{cell}	applied single cell voltage (V)
F	Faraday constant ($=96\,485.309$ C mol^{-1})

H_i	Henry's constant of species (mol cm^{-3} atm^{-1})
I	total current density of single cell (A cm^{-2})
I_L	limiting current density of single cell (A cm^{-2})
i	local current density (A cm^{-2})
i_0	exchange current density (A cm^{-2})
k_{scx}	salting out coefficient (cm^3 mol^{-1})
L	thickness of layer (cm)
M_i	molecular weight of species i (mg mol^{-1})
N_i	molar flux of species i (mol cm^{-2} s^{-1})
n	number of electron transferred
P_i	partial pressure of species i (atm)
q_i	reaction order of species i
R	ideal gas constant (= 8.31451 J mol^{-1} K^{-1})
R_i^e	electrochemical reaction rate of species i (mol cm^{-3} s^{-1})
R_i^p	mass-transfer rate of species i across phase boundary (mol cm^{-3} s^{-1})
R_{ohm}	slope of polarization curve in ohmic polarization region (Ω cm^2)
s_i	stoichiometric coefficient of species i
T	temperature (K)
t	time (s)
t_i	transferrence number of species i
U	open-circuit potential (V vs. SHE)
u_i	mobility of species i (mol cm^2 J^{-1} s^{-1})
$\mathscr{u}_i$	effective mobility of species i (mol cm^2 J^{-1} s^{-1})
V	specific volume of layer (cm^3 mg-cat^{-1})
$\overline{V}_i$	partial molar volume of species i (cm^3 mol^{-1})
v ■	volume average velocity (cm s^{-1})
v_i	velocity of species i (cm s^{-1})
x_i	liquid phase mole fraction of species i
x_i^0	liquid phase mole fraction of species i in pure water
y_i	vapour phase mole fraction of species i
z	spatial coordinate (cm)
z_i	charge number of species i

Greek

α_a	apparent anodic transfer coefficient
α_c	apparent cathodic transfer coefficient
δ	thickness of electrolyte film (cm)
ε	porosity
ζ	dimensionless spatial coordinate
η	local overpotential (V)
κ	electrical conductivity (S cm^{-1})
κ_e	ionic conductivity of electrolyte (S cm^{-1})
Λ	equivalent conductance (cm^2 Ω^{-1} eq^{-1})
Λ^0	limiting equivalent conductance (cm^2 Ω^{-1} eq^{-1})
λ_i	ionic equivalent conductance of ion i (cm^2 Ω^{-1} eq^{-1})
λ_i^0	limiting ionic equivalent conductance of ion i (cm^2 Ω^{-1} eq^{-1})
ν	number of times of the rate determining step occur for overall reaction occur once
ν_i	number of cations or anions produced by the dissociating electrolyte
σ	effective electrical conductivity (S cm^{-1})
τ	tortuosity
Φ	solution phase potential (V)

Superscripts

a	anode
c	cathode
g	gas phase
l	liquid phase
e	electrochemical reaction
r	reference condition
p	mass transfer across a phase boundary
TF	PTFE
s	electrically conductive solid phase
θ	standard condition

Subscripts

a	anode
c	cathode
CL	catalyst layer
aCL	anode catalyst layer
cCL	cathode catalyst layer
e	electrolyte
GDL	gas-diffusion layer
aGDL	anode gas-diffusion layer
cGDL	cathode gas-diffusion layer
H	H_2
i	species i
j	species j
O	O_2
SEP	separator layer
w	H_2O
+	cation (K^+)
−	anion (OH^-)

Acknowledgements

The authors are grateful to the CPRC (Ceramic Processing Research Center) of Hanyang University, Korea, for partial support of this work.

References

[1] G. Suljak, Program and Abstracts: 1994 Fuel Cell Seminar, San Diego, CA, 1994, p. 415.
[2] S.S. Penner, Assessment of Reserch Needs for Advances Fuel Cells, Pergamon, NY, 1986, p. 147.
[3] P. Bjornbom, S.-C. Yang, Electrochim. Acta 38 (1993) 2599.
[4] M.C. Kimble, R.E. White, J. Electrochem. Soc. 138 (1991) 3370.
[5] J. Newman, W. Tiedemann, AIChE J. 21 (1975) 25.

[6] K. Kordesch, G. Simader, Fuel Cells and Their Applications, VCH Publishers, NY, 1996, p. 62.
[7] M.C. Kimble, Ph.D. Thesis, Texas A&M University, College Station, TX, 1991.
[8] R.B. Bird, W.E. Stewart, E.N. Lightfoot, Transport Phenomena, Wiley, NY, 1960, p. 518, p. 505.
[9] J.S. Newman, Electrochemical Systems, Prentice-Hall, Englewood Cliffs, NJ, 1973, p. 532.
[10] O. Fuhrer, Dr.rer.nat. Dissertation, Gesamthochschule Kassel, 1990.
[11] J. Isaelachvili, Intermolecular and Surface Forces, Academic Press, San Diego, CA, 1991, p. 55.
[12] R.C. Reid, J.M. Prausnitz, B.E. Poling, The Properties of Gases and Liquids, McGraw-Hill, NY, 1987, p. 336.
[13] S.K. Shoor, R.D. Walker Jr., K.E. Gubbins, J. Phys. Chem. 73 (1969) 312.
[14] M.K. Tham, R.D. Walker, K.E. Gubbins, J. Phys. Chem. 74 (1970) 1747.
[15] R.N. Bhatia, K.E. Gubbins, R.D. Walker, Trans. Faraday Soc. 64 (1968) 2091.
[16] A.L. Horvath, Handbook of Aqueous Electrolyte Solutions: Physical Properties, Estimation and Correlation Methods, Ellis Horwood, Chichester, England, 1985, pp. 262–263, p. 252.
[17] E. Gileadi, Electrode Kinetics, VCH Publishers, NY, 1993, p. 130.
[18] B.V. Tilak, P.W.T. Lu, J.E. Colman, S. Srinivasan, in: J.O'M. Bockris, B.E. Conway, E. Yeager, R.E. White (Eds.), Comprehensive Treatise of Electrochemistry, Vol. 2, Plenum, New York, 1984, pp. 18–24.
[19] K. Kinoshita, Electrochemical Oxygen Technology, Wiley, NY, 1992, pp. 37–40.
[20] J.-H. Jo, S.-C. Yi, S.-K. Moon, Hwahak Konghak 35 (1997) 838.
[21] A. Winsel, G.J. Richter, in: H. Wendt (Ed.), Electrochemical Hydrogen Technologies, Elsevier, NY, 1990, p. 411.
[22] J. Singer, W.L. Fielder, J. Power Sources 29 (1990) 443.
[23] T. Kenjo, J. Electrochem. Soc. 133 (1986) 2051.
[24] L. Qingfeng, X. Gang, H.A. Hjuler, R.W. Berg, N.J. Bjerrum, J. Electrochem. Soc. 141 (1994) 3114.
[25] J. Newman, Ind. Eng. Chem. Fundam. 7 (1968) 514.
[26] R.E. Martin, M.A. Manzo, Paper 889498, 23rd Intersociety Energy Conversion Engineering Conference, 1988.
[27] K. Strasser, J. Power Sources 29 (1990) 149.
[28] H. van den Broeck, in: L.J.M.J. Blomen, M.N. Mugerwa (Eds.), Fuel Cell Systems, Plenum, New York, 1993, p. 42, p. 250.
[29] P. Ruetschi, R.F. Amile, J. Phys. Chem. 70 (1966) 718.
[30] R.E. Davis, G.L. Horvath, C.W. Tobias, Electrochim. Acta 12 (1967) 287.
[31] S. Srinivasan, D.J. Manko, H. Koch, M.A. Enayetullah, A.J. Appleby, J. Power Sources 29 (1993) 367.